The influence of heterogeneity on the strength of volcanic rocks and the stability of lava domes

Michael Heap, Claire Harnett, Tofig Nazarbayov, Zhen Heng, Patrick Baud, Tao Xu, Marina Rosas-Carbajal, Jean-Christophe Komorowski

The influence of heterogeneity on the strength of volcanic rocks and the stability of lava domes

Michael J. Heap[1,2]*, Claire E. Harnett[3*], Tofig Nazarbayov[4,1], Zhen Heng[5], Patrick Baud[1], Tao Xu[5], Marina Rosas-Carbajal[6], and Jean-Christophe Komorowski[6]

[1] *Université de Strasbourg, CNRS, Institut Terre et Environnement de Strasbourg, UMR 7063, 5 rue Descartes, Strasbourg F-67084, France*

[2] *Institut Universitaire de France (IUF), Paris, France*

[3] *UCD School of Earth Sciences, University College Dublin, Dublin, Ireland*

[4] *French-Azerbaijani University (UFAZ), Nizami Str. 183, Baku, Azerbaijan*

[5] *School of Resources and Civil Engineering, Northeastern University, Shenyang, 110819, China*

[6] *Université de Paris, Institut de Physique du Globe de Paris, CNRS, F-75005 Paris, France*

*Corresponding authors: Michael Heap (heap@unistra.fr) and Claire Harnett (claire.e.harnett@ucd.ie)

ORCID

MJ Heap (0000-0002-4748-735X)

CE Harnett (0000-0002-7089-7875)

T Nazarbayov

Zhen Heng

P Baud (0000-0002-4728-7649)

Tao Xu (0000-0001-8971-674X)

Marina Rosas-Carbajal (0000-0002-5393-0389)

Jean-Christophe Komorowski (0000-0002-6874-786X)

Abstract

The collapse of lava domes, inherently heterogeneous structures, represents a significant volcanic hazard. Numerical and analogue models designed to model dome instability and collapse have incorporated heterogeneity

in the form of discrete zones with homogeneous properties. Based on an assessment of dome rock heterogeneity, we explore whether material property heterogeneity ("diffuse" heterogeneity) within these discrete zones can promote dome instability. X-ray computed tomography shows that dome samples are characterised by high microstructural heterogeneities; e.g., porosity varies from 0.07 to 0.20 over millimetric lengthscales. To explore how microstructural heterogeneity influences sample-scale strength, we performed numerical simulations using Rock Failure and Process Analysis. The mean mechanical properties of the numerical samples were constant, and we introduced heterogeneity by varying their distribution using a Weibull probability function. The models show that increasing heterogeneity can reduce sample-scale strength by more than a factor of two. To explore the influence of dome-scale heterogeneity, we numerically generated lava domes in Particle Flow Code. The domes have the same bulk strength but are characterised by different degrees of heterogeneity by varying the distribution of cohesion using a Weibull probability function. The models show that a greater degree of heterogeneity induces higher dome-scale displacements and that, when there is also a discrete weakened zone, the addition of diffuse heterogeneity leads to more widely distributed deformation. Therefore, alongside discrete zones defined by different material properties, we find that the diffuse heterogeneity inherent to a dome is sufficient to compromise dome stability and should be incorporated in future modelling endeavours.

Keywords: lava dome; heterogeneity; uniaxial compressive strength; porosity; coefficient of variation

1 Introduction

The collapse of a lava dome, which can result in rock falls, debris avalanches, laterally-directed explosions, and pyroclastic density currents, represents a significant volcanic hazard (Sparks, 1997; Nakada et al., 1999; Voight, 2000; Voight et al., 2000; Voight and Elsworth, 2000; Calder et al., 2002; Saucedo et al., 2005; Komorowski et al., 2013; Ogburn et al., 2015; Harnett et al., 2019a). The collapse of a lava dome can also rapidly depressurise subsurface magma, triggering large and potentially devastating eruptions (Sparks et al., 2002). The mechanisms of dome instability are numerous, and very often operate in concert. For example, dome stability can be compromised by increases in magma extrusion rate (Calder et al., 2002), basal strike-slip movements (Lagmay et al., 2000), the build-up of pressurised fluids (Sparks, 1997; Komorowski et al., 1997; Voight and Elsworth, 2000; Reid, 2004; Ball et al., 2018; Heap et al., 2021a; Mordensky et al., 2022), topographical, geometrical, and structural factors (Walter et al., 2015; Darmawan et al., 2018; Harnett and Heap, 2021, Mériaux et al., 2022), ground acceleration resulting from earthquakes (Wallace et al., 2021), hydrothermal alteration (Reid et al., 2001;

Ball et al., 2013; Heap et al., 2021b; Darmawan et al., 2022; Harnett et al., 2022), and rain-induced pore-fluid pressurisation (Matthews et al., 2002; Elsworth et al., 2004; Taron et al., 2007).

A characteristic common to all lava domes is that they are heterogeneous across a variety of scales. At the microstructural scale (tens to hundreds of microns), microscopy and X-ray computed tomography have shown that volcanic rocks, including dome rocks, are heterogeneous, typically containing a groundmass populated by phenocrysts and pores in variable quantities and of variable sizes and shapes (Zandomeneghi et al., 2010; Shea et al., 2010; Kushnir et al., 2016; Farquharson et al., 2016; Rhodes et al., 2018; Cashman, 2020). Moreover, the observation of micro-breccia and micrometre-size pyroclast-filled fractures (tuffisites) in cryptodomes and lavas (Heiken et al., 1988; Komorowski et al., 1997; Tuffen et al., 2003) are evidence of the presence of textural discontinuities and the circulation of pressurised gas that may generate variations in mechanical properties and, therefore, heterogeneity. At the sample scale (a few to tens of centimetres), laboratory studies have shown that the physical and mechanical properties of rocks collected from the same dome can vary by several orders of magnitude (Smith et al., 2011; Heap et al., 2014a; Farquharson et al., 2015; Harnett et al., 2019b; Bain et al., 2019; Heap et al., 2020a; Kendrick et al., 2021; Heap and Violay, 2021). The large range in the physical and mechanical properties typically observed for volcanic rocks of the same porosity is often considered to be the result of micro- and sample-scale heterogeneities (e.g., Heap and Violay, 2021). Numerical experiments using modelling software Fast Lagrangian Analysis of Continua (FLAC; Itasca Consulting Group Ltd) (Villeneuve et al., 2012), UDEC and 3DEC (Distinct Element Modelling; Itasca Consulting Group Ltd) (Ghazvinian et al., 2014; Stavrou et al., 2019; Xu et al., 2020), Rock Failure Process Analysis (RFPA; Mechsoft Technology) (Tang et al., 2000, 2007; Zhu, 2008), and Particle Flow Code (PFC; Itasca Consulting Group Ltd) (Peng et al., 2017; Liakas et al., 2017) have also demonstrated that microstructural heterogeneity leads to a reduction in rock strength. Numerical experiments have also shown that pore size and shape (Heap et al., 2014b; Griffiths et al., 2017; Heap et al., 2021c) and crystal content (Heap et al., 2016) can influence mechanical behaviour of volcanic rocks.

At the dome-scale (tens to hundreds of metres), field investigations and analogue and numerical modelling have shown that lava domes are structurally very complex, with mechanical properties that vary through space and time (Fink and Griffiths, 1998; Watts et al., 2002; Harnett et al., 2019b; Zorn et al., 2020; Tsepelev et al., 2021). Geophysical methods have also exposed the large-scale heterogeneity of lava domes. For example, muon tomography—a geophysical method that can provide the 3D density structure of a volcano—has shown that the density of a dome can be spatially very variable (Tanaka et al., 2007; Lesparre et al., 2012; Rosas-Carbajal et al., 2017), corresponding to spatial variations in compressive and tensile strength (Heap et al., 2021b). Electrical

resistivity and magnetic surveys have shown that portions of a lava dome can be affected by the presence of a hydrothermal system, the location and/or extent of which can depend on internal structural features (Rosas-Carbajal et al., 2016; Byrdina et al., 2017; Finn et al., 2018; Peterson et al., 2021). Heterogeneity is commonly reflected in numerical and analogue models of volcanoes and volcanic domes, typically designed to better understand large-scale deformation (e.g., slow spreading, sliding on pre-existing faults or fractures, the formation of large-scale fractures, partial collapse), as discrete zones defined by different material properties. For example, analogue models have used different materials—silicon putty to represent weakened or altered zones and a sand-gypsum mixture to represent stronger and/or intact zones—to represent different discrete zones within the volcano (Cecchi et al., 2004; van Wyk de Vries et al., 2000, Byrne et al., 2013). Numerical models typically separate the volcanic edifice, flank, or dome into different discrete zones, often guided by geophysical data, and assign these zones different rock physical and mechanical properties (Heap et al., 2021b; Harnett and Heap, 2021; Carr et al., 2022; Harnett et al., 2022; Mordensky et al., 2022). An example of this *discrete heterogeneity* is shown in Fig. 1a, where a lava dome is split into two discrete zones characterised by different, but uniform, physical and mechanical properties (a weak zone in yellow and a strong zone in white). In the context of a volcanic edifice, flank, or dome, such discrete zones could represent, for example, volumes that are characterised by different rock types with different properties, different lava units, different domes or spines within a dome complex, or zones variably influenced by hydrothermal alteration. However, existing geophysical datasets suggest that, although volcanic structures can, and should, be considered with discrete zones characterised by different physical and mechanical properties, these properties also vary within these discrete zones (termed here as *diffuse heterogeneity*). An example of *discrete and diffuse heterogeneity* is shown in Fig. 1b, where the lava dome is again split into two discrete zones characterised by different physical and mechanical properties (i.e. *discrete heterogeneity*) but, in this instance, the physical and mechanical properties within these zones are also heterogenous (i.e. *diffuse heterogeneity*). However, the extent to which diffuse heterogeneity can influence dome stability remains unexplored.

Our goal in this contribution is to better understand the role of heterogeneity on the stability of a lava dome. We first characterised the microstructural heterogeneity of dome rocks using X-ray micro computed tomography (μCT). We then performed numerical experiments, calibrated using laboratory stress-strain data for dome rock, to assess the influence of systematically varied microstructural heterogeneity on the strength of dome rocks at the sample-scale. Finally, we investigated the effect of heterogeneity at the dome scale. To do so, we simulated domes characterised by the same average bulk strength, but with different heterogeneities (i.e. diffuse

heterogeneity), and domes characterised by both discrete and diffuse heterogeneities. These results reveal new insights on the influence of the internal structure and fabric of volcanic domes on their stability. As such they are aimed at providing one of the missing links to progress beyond the state of the art of modelling and the quantitative evaluation of dome volumes susceptible to instability and collapse and the modelling of resulting rockslide and debris avalanche emplacement as proposed by, for example, Peruzzetto et al. (2019). Understanding the mechanisms that can contribute to dome instability and collapse will help improve monitoring strategies and mitigate the hazards presented by lava domes worldwide.

2 Materials and Methods

2.1 Microstructural and compositional heterogeneity

To assess the microstructural heterogeneity of dome rocks, X-ray tomography images were acquired for cylindrical samples (10 mm in diameter and 20 mm in length) prepared from three dome rocks from La Soufrière de Guadeloupe, an active andesitic stratovolcano located on the French island of Guadeloupe in the Eastern Caribbean (Moretti et al., 2020). Two of the three dome rocks were collected from a collapse scar to the northeast of dome summit (samples H3 and H4A), and the third was collected from the dome summit near Cratère Sud (sample H19). Samples from these blocks were recently analysed in terms of their compressive and tensile strength (Heap et al., 2021b, 2022a, b) and thermal properties (Heap et al., 2022c). Fig. 2 shows backscattered scanning electron microscope (SEM) images of each sample. All three dome rocks are porphyritic andesites characterised by a microcrystalline groundmass with phenocrysts of dominantly plagioclase and pyroxene (orthopyroxene and clinopyroxene) (Fig. 2). The connected porosity of each of the three cylindrical samples was calculated using their bulk sample volumes and their skeletal (connected) volumes measured using a helium pycnometer. The connected porosities were measured to be 0.18, 0.20, and 0.12 for samples H3, H4A, and H19, respectively.

X-ray tomography images were acquired for the three cylindrical samples at the High-Resolution X-ray Computed Tomography Facility at the University of Texas at Austin (USA). X-rays were set to 90 kV and 12 W, and the acquisition time was 0.07 s. A total of 4175 image slices, with a voxel side length of 5 μm, were taken of each of the three cylindrical samples.

X-ray powder diffraction (XRPD) was used to provide the mineral content of all three samples (data from Heap et al., 2021b, 2022c). These XRPD data reveal that all three samples are characterised by advanced argillic alteration, the result of the efficient circulation of acidic sulfate-chloride-rich fluids (below 350 °C, and down to 150–200 °C; pH < 4) (Heap et al., 2021b). Sample H3 contains primary plagioclase (46.6 wt%), pyroxene (11.8

and 5.6 wt% of orthopyroxene and clinopyroxene, respectively), and magnetite (0.8 wt%); secondary minerals include kaolinite (17.4 wt%), cristobalite (10.6 wt%), pyrite (3.8 wt%), Na-alunite (2.8 wt%), and quartz (0.6 wt%). Sample H4A contains primary plagioclase (23.3 wt%) and pyroxene (11.8 and 4.9 wt% of orthopyroxene and clinopyroxene, respectively); secondary minerals include kaolinite (43.4 wt%), cristobalite (11.8 wt%), pyrite (2.3 wt%), Na-alunite (1.3 wt%), gypsum (0.7 wt%), and quartz (0.6 wt%). Sample H19 contains primary plagioclase (22.0 wt%) and pyroxene (10.2 and 5.0 wt% of orthopyroxene and clinopyroxene, respectively), secondary minerals include opal-A (33 wt%), Na-alunite (14.2 wt%), cristobalite (9.5 wt%), hematite (2.4 wt%), kaolinite (2.0 wt%), and quartz (1.7 wt%). In all three samples, Na-alunite and cristobalite are observed as pore-filling precipitates and plagioclase phenocrysts are often altered and partially replaced by opal-A and/or kaolinite (Fig. 2). The total wt% of secondary (alteration) minerals, a measure of their alteration, in samples H3, H4A, and H19 is 35.2, 60, and 62.8 wt%, respectively. We highlight that, although these hydrothermally altered samples are representative of the material forming the dome at La Soufrière de Guadeloupe, they may not represent freshly extruded dome materials at other active volcanoes that can be characterised by initially low levels of alteration.

2.2 Sample scale heterogeneity: Rock Failure and Process Analysis modelling

To explore the effect of heterogeneity on the sample scale, 2D numerical experiments were performed using Rock Failure and Process Analysis (RFPA), a numerical code based on elastic damage mechanics (Tang, 1997, 2011). Numerical samples were prepared to the same dimensions as the uniaxial compressive strength tests performed in Heap et al. (2021b), which were 20 mm in diameter and 40 mm in length. Before we performed the numerical experiments, we ran some preliminary simulations to ascertain the appropriate mesh size for the model. To do so, we performed simulations with the aim of using the model to capture stress-strain data from a laboratory experiment performed on a sample of andesite from La Soufrière de Guadeloupe (sample H18; Heap et al., 2021b) in which the numerical samples consisted of either 45,000 or 80,000 square elements, resulting in resolutions of 7.5 and 10 elements per mm, respectively. Both of these simulations accurately captured the mechanical behaviour of the laboratory experiment and so we used numerical samples containing 45,000 square elements (resolution of 7.5 elements per mm) for our numerical experiments. In the model, each square element is assigned a set of physical and mechanical input parameters. To obtain the mean values for these model input parameters, we performed a calibration in which we modified the model input parameters until the stress-strain behaviour, Young's modulus, and uniaxial compressive strength from the numerical experiment matched that of a laboratory experiment performed on a sample of andesite from La Soufrière de Guadeloupe (sample H18; Heap et al., 2021b).

The stress-strain curves for the numerical and laboratory experiment are shown in Fig. 3a, and the mean input parameters for the calibrated model are listed in Table 1. For the calibration model, the physical and mechanical properties of each square element were not identical, and varied according to a Weibull probability density function:

$$x(u) = \frac{m}{u_0}\left(\frac{u}{u_0}\right)^{m-1} exp\left[-\left(\frac{u}{u_0}\right)^{m}\right]. \quad (1)$$

A Weibull probability density function contains a scale parameter and a shape parameter. Here, u is the scale parameter of an individual element, and the scale parameter u_0 is the average element parameter. $x(u)$ is the dependence of a given property on the distribution scale input, u, such that $x(u)$ is replaced by the Young's modulus, $E_0(u)$, or the uniaxial compressive strength, $\sigma_c(u)$, to determine the probability of a certain square element having a certain property. The shape parameter is m. In material sciences, the shape parameter m is often called the "*homogeneity index*". For the calibration model, we set m to be 5. As a result, although the mean uniaxial compressive strength of an element in the numerical experiment shown in Fig. 3a was 147.3 MPa (Table 1), the strength of an individual element varied according to Eq. (1), where m = 5. This microscale heterogeneity resulted in a numerical sample with a macroscopic uniaxial compressive strength of 98.8 MPa (Fig. 3a). Therefore, changing homogeneity index, m, and keeping all the other parameters in the model constant, allows us to explore the influence of microscale heterogeneity on sample-scale uniaxial compressive strength, where high values of m correspond to very homogeneous samples, and low values of m correspond to very heterogeneous samples. An extremely high homogeneity index yields a Gaussian distribution with high kurtosis (Xu et al., 2018). As the homogeneity index decreases, the distribution becomes increasingly positively skewed (Fig. 3b). Indeed, although the mean values remain constant, the median values of uniaxial compressive strength and Young's modulus decrease as a function of decreasing homogeneity index. For example, at m = 1.1, the median uniaxial compressive strength and Young's modulus are 105.7 MPa and 33.2 GPa, respectively. Owning to their success in simulating the mechanical behaviour and failure of rock, the statistics of the mechanical properties of rock are often assumed to follow Weibull distributions in numerical modelling (Tang, 1997; Zhu and Tang, 2004; Liu et al., 2004; Wong et al., 2006; Tang, 2011). Weibull distributions have also been used in other aspects of volcanology. For example, Weibull functions have been used to describe the distribution of dyke thickness (Krumbholz et al., 2014) and the distribution of flaws surrounding magma chambers (Gray and Monaghan, 2004).

We performed numerical experiments in which deformed samples were characterised by different values of m: 1.1 (most heterogeneous), 2, 3, 4, 5, 6, 7, and 8 (most homogeneous). The distribution of Young's modulus (mean value of 46 GPa; Table 1) and uniaxial compressive strength (mean value of 147.3 MPa; Table 1) for each of these numerical experiments are shown in Figs. 3b and 3c, respectively. For example, as shown in Fig. 3c, the elements comprising the sample with the highest value of m are clustered around the mean value of 147.3 MPa, whereas the elements comprising the sample with the lowest value of m can be much lower (close to 0 MPa) or much higher (higher than 350 MPa) than this mean value. We note that the microstructural heterogeneity in our numerical samples is provided by varying the physical and mechanical properties of square elements that have a length of 133 μm and, as a result, the modelling assumes microstructural heterogeneities of the same size. In nature, and in our dome samples (Fig. 2), volcanic rocks can contain heterogeneities on a number of scales, from the nano- or microscale to the scale of the sample (centimetric scale). The influence of larger heterogeneities, such as mm-scale pores (Heap et al., 2014b; Griffiths et al., 2017; Heap et al., 2021c) and crystals (Heap et al., 2016), on the mechanical behaviour of volcanic rocks have been investigated in previous studies using a heterogeneous groundmass with a constant homogeneity index (m = 3). The modelling presented here varies the homogeneity index of the groundmass in numerical samples (m = 1.1, 2, 3, 4, 5, 6, 7, and 8) that do not contain larger pores and crystals, or any other mm-scale heterogeneity.

2.3 Dome scale heterogeneity: Particle Flow Code modelling

To explore the effect of heterogeneity on the dome scale, we used 2D Discrete Element Method (DEM) models created in Particle Flow Code (PFC; Itasca Consulting Group Ltd), following the methods outlined by Harnett et al. (2018) and Harnett and Heap (2021). The DEM allows us to model the post-failure detachment and movement of blocks of rock, which cannot be simulated by the FEM-based software RFPA used for the sample-scale modelling. We suggest that DEM modelling is therefore more relevant for dome-scale simulations due to the spectrum of collapse processes that can be expected at natural domes (e.g., Calder et al., 2002). Indeed, PFC modelling has been previously, and successfully, used to model dome growth and collapse (Husain et al., 2014; Harnett et al., 2018; Harnett and Heap, 2021; Harnett et al., 2022). These DEM models consider a particle-based material in which circular particles interact at interparticle contacts. Contact behaviour is primarily governed by stiffness and cohesion. At the boundary between the particles and walls (i.e. the ground surface), the contact behaviour is cohesionless and governed by friction. The particle size in the model is not representative of individual crystals, grains, or rock blocks, but rather represents discretisation of the medium for the purpose of computation.

First, we numerically generated two fully solid domes (see Harnett and Heap, 2021) containing 9745 circular particles and 22710 contacts. These contacts are given a uniform strength of 1 MPa. We select here a much lower bulk strength for the dome-scale (1 MPa) than the sample-scale (tens to hundreds of MPa) following previous studies that have shown that a decrease in magnitude is required when upscaling laboratory parameters for use at the dome-scale (Walter et al., 2019; Villeneuve and Heap, 2021). The domes are stable, such that they will not deform unless perturbed in some way.

To explore the effect of heterogeneity on the stability of a dome, we used the Weibull probability density function shown in Eq. 1 to provide a distribution of the cohesion parameter acting at each interparticle contact. For one dome, we let m = 2, creating a heterogenous dome, where the lowest contact cohesion is close to 0 MPa (representative of weak or altered rock) and the highest contact cohesion is 3 MPa (representative of strong or fresh rock). For the other dome, we let m = 10, creating a relatively homogeneous dome, where the contact cohesion values cluster more tightly around 1 MPa, with minimum cohesion values of ~0.5 MPa and maximum cohesion values of <1.5 MPa. In both cases, the average strength remains equal (i.e., the mean bond strength is 1 MPa in both cases), allowing us to solely explore the influence of heterogeneity on dome strength. In each case, we vary both the cohesive and tensile strength as a function of the Weibull distribution, where the compressive to tensile strength ratio is constant at 10:1 (Heap et al., 2022a). The distributions of bond cohesion for the two domes are shown in Fig. 4.

3 Results

3.1 Microstructural and compositional heterogeneity

We used X-ray micro computed tomography (μCT) to assess the microstructural and compositional heterogeneity of three dome samples from La Soufrière de Guadeloupe. Using open-source software ImageJ, we first plot grey level histograms for each sample using the entire μCT image volumes (Fig. 5). The grey level is a value between 0 (lowest attenuation and lowest density) and 255 (highest attenuation and highest density). The three dome rocks are characterised by three peaks: at values of grey level of ~20, ~45−50, and ~90−95 (Fig. 5). Although we consider the peak at a grey level of ~20 contains to correspond to the porosity within the sample, this peak also includes voxels that contain both porosity and solid material (groundmass and/or crystals). The peaks at grey levels of ~45−50 and ~90−95 likely correspond to, respectively, the groundmass and higher-density crystals (e.g., plagioclase crystals that are denser than the groundmass). The broad nature of these peaks, and the saddles

between them, are likely the result of voxels containing mixtures of groundmass and crystals. The wide variation in grey level, and therefore density, within the samples speaks to their high microstructural heterogeneity.

Next, we stacked the μCT images in ImageJ and determined the coefficient of variation (COV) of the grey level (the ratio of the standard deviation of the grey level to the mean grey level), the porosity, the average equivalent pore diameter, the average pore aspect ratio, and the average pore circularity for each image in the stack (a total of 4175 image slices). The COV of the grey level in μCT images of rocks has previously been used to assess microstructural heterogeneity (e.g., Louis et al., 2007). In these analyses, and due to edge effects, we removed 300 slices (i.e. 1.5 mm) from the top and bottom of each of the stacks. The equivalent pore diameter, d, was determined using $d = (3/2)d_F$, where d_F is the average Feret diameter. The pore aspect ratio is the ratio of the minor to major pore axis, where a perfect circle would have an aspect ratio of one. Finally, the pore circularity, C, is given by $C = 4\pi p^2$, where p is the pore perimeter. A perfect circle will have a pore circularity of one. In all the analyses of pore size and shape, we excluded all pores that were determined to have a diameter < 10 μm.

Using the voxel side length of 5 μm as the thickness of each image, we can plot these microstructural parameters as a function of sample length. We plot the COV and porosity as a function of sample length for each of the three dome samples in Figs. 6 and 7, respectively (plots for the average equivalent pore diameter, the average pore aspect ratio, and the average pore circularity are provided in the Supplementary Information). We also provide the image slice with the highest and lowest value for each sample in Figs. 6 and 7. Fig. 6 shows that the COV varies from 0.27−0.31 to 0.48−0.52, and that the variation in COV is approximately the same for each of the three samples. The image slices with the lowest values of COV are those without high-density pyrite and hematite and with few plagioclase phenocrysts (Fig. 6). Conversely, the image slices with the highest values of COV are those with large amounts of high-density pyrite and hematite and large plagioclase phenocrysts (Fig. 6). Fig. 7 shows that the porosity of samples H3, H4A, and H19 varies from 0.07−0.20, 0.04−0.10, and 0.05−0.11, respectively. The image slices with the lowest and highest porosities are those with a small and large number of macropores, respectively (Fig. 7). The average porosity calculated from the stacked CT images are 0.11, 0.07, and 0.08 for H3, H4A, and H19, respectively (Fig. 7). These calculated porosities are lower, and much lower in the case of H4A, than the connected porosities measured in the laboratory (0.18, 0.20, and 0.12 for H3, H4A, and H19, respectively). The lower porosities calculated using the CT images, compared to the laboratory-measured values, is the result of the presence of < 10 μm-diameter micropores that are, presumably, abundant in sample H4A.

We find that the average equivalent pore diameters of samples H3, H4A, and H19 are 82, 63, and 99 μm, respectively. The average pore aspect ratio of each sample is 0.52. And, finally, the average pore circularities of

samples H3, H4A, and H19 are 0.73, 0.74, and 0.68, respectively. We find that the equivalent pore diameter, the pore aspect ratio, and the pore circularity do not vary considerably along the sample lengths (see data in Supplementary Information). Although the proportion and size of the macropores varies from slice to slice (see the image slices in Fig. 7), the large number of smaller pores results in a similar average equivalent pore diameter for each of the slices along the length of the samples.

3.2 Impact of heterogeneity on the sample scale

To explore the effect of microstructural and compositional heterogeneity on the sample scale, we performed calibrated 2D numerical experiments using RFPA. The samples in these numerical experiments were all characterised by the same average Young's modulus and strength, but we varied their homogeneity by changing the range of these two parameters using a Weibull probability density function (Fig. 2; Eq. 1). The results of the numerical experiments are shown in Fig. 8 (see also Table 2). We first note that all the numerical samples failed in a brittle manner, whereby sample failure was promoted by the formation of a throughgoing macroscopic fracture (see inset on Fig. 8b). The data of Fig. 8 show that the uniaxial compressive strength of the numerical samples decreases from ~110 MPa at a homogeneity index of 8 (the most homogeneous sample) to ~45 MPa at a homogeneity index of 1.1 (the most heterogeneous sample). In other words, increasing sample heterogeneity can reduce sample-scale strength by more than a factor of two. Fig. 8 also shows that the reduction in strength as the homogeneity index is decreased is non-linear: strength is decreased by only a couple of MPa when the homogeneity index is decreased from 8 to 7, but decreases by almost 20 MPa when the homogeneity index is decreased from 2 to 1.1 (see also Table 2). We also highlight that the post-peak portion of the numerical experiments performed at m = 7 and 8 are different to those performed at lower values of m (Fig. 8). The stress drop associated with macroscopic sample failure at $m < 7$ occurs almost immediately after the peak stress is reached whereas, at $m = 7$ and 8, the sample reaches the peak and there is an appreciable strain softening period prior to the stress drop that accompanies macroscopic failure (Fig. 8).

3.3 Impact of heterogeneity on the dome-scale

To explore the effect of heterogeneity at the dome scale, we performed 2D simulations using PFC. The model starting condition in each stage is a quasi-stable dome, which has already settled under gravitational forces and will not deform unless intrinsic or extrinsic factors are changed. The initial modelled dome has a width of 440 m and a maximum height of 130 m. The new models presented here show domes characterised by the same average

bond cohesion; this is analogous to the uniaxial compressive strength of the macroscale material. To explore the influence of heterogeneity, we prepared a reasonably homogenous dome (for which $m = 10$; Fig. 4; Eq. 1) and a very heterogeneous dome (for which $m = 2$; Fig. 4; Eq. 1). The distribution of bond cohesion in these models is shown in Fig. 9. The domes analysed in this study are unbuttressed domes that were emplaced on a flat surface (Fig. 9).

The influence of dome heterogeneity on an otherwise-stable dome is presented in Fig. 10. The images in Fig. 10 show the displacement in the dome when the contact cohesion between particles was changed from a uniform value of 1 MPa (the quasi-stable dome; perfectly homogeneous in terms of particle contact cohesion) to values assigned by the Weibull probability function (mean bond strength in both scenarios is 1 MPa; but contact cohesion varies from ~0.5 MPa to <1.5 MPa for the relatively homogenous dome (Fig. 10a) and from close to 0 MPa to 3 MPa for the heterogeneous dome (Fig. 10b)). The average displacement is 0.0036 m for the relatively homogenous dome (Fig. 10a) and 0.0198 m for the heterogeneous dome (Fig. 10b). The dome with higher heterogeneity shows higher displacements across the dome, and particularly at its centre (Fig. 10b), and shows that heterogeneity alone is enough to destabilise the dome, even when the bulk strength remains equal. By contrast, the relatively homogeneous dome remains stable, with only minor displacements toward the left flank of the dome (Fig. 10a).

4 Discussion

4.1 Microstructural heterogeneity of volcanic rocks

Our SEM images (Fig. 2) and μCT data (Figs. 5, 6, and 7) have shown that dome rocks can be characterised by a high degree of microstructural heterogeneity. As a comparison, the COV values calculated for the four sandstones analysed in Louis et al. (2007), using images acquired at a very similar resolution to those presented here (a voxel side length of 5.7 μm, compared to 5 μm for the images acquired for this study), were 0.186, 0.255, 0.303, and 0.313, respectively. The maximum COV values determined for our three dome rocks were 0.48, 0.52, and 0.51 for H3, H4A, and H19, respectively (Fig. 6). The domes rock from La Soufrière de Guadeloupe were also characterised by three broad X-ray attenuation coefficient peaks associated with macropores, plagioclase phenocrysts, and high-density Fe-Ti oxides (Fig. 5), as also observed for dome rock from Volcán de Colima (Mexico; Heap et al., 2020b). By contrast, X-ray attenuation coefficient peaks in porous sandstones are typically strongly bimodal, with narrow peaks associated with macropores and grains (Louis et al., 2007). Two X-ray attenuation coefficient peaks are also observed in porous limestones (Ji et al., 2015). We note

that the range of COV values for the more altered dome rocks (H4A and H19; characterised by an alteration of 60 and 62.8 wt.%, respectively) is larger than for the least altered dome rock (H3; characterised by an alteration of 35.2 wt.%) (Fig. 6), suggesting that hydrothermal alteration may increase the heterogeneity of dome rock (although more data are now required to test this hypothesis).

The variation in porosity along the length of a 10 mm-long sample of dome rock is particularly noteworthy (Fig. 7). We find that the porosity of samples H3, H4A, and H19 varies from 0.07−0.20, 0.04−0.10, and 0.05−0.11, respectively (Fig. 7). For comparison, the porosity measured using μCT data along the length of sandstone samples was found to be ~0.04 ± 0.002 (Long et al., 2009), ~0.3 ± 0.03 (Appoloni et al., 2007), and the porosity of a suite of low-porosity (< 0.1) sandstones was found to vary by up to about ± 0.025 (Zhao et al., 2019). The porosities of three porous limestones were found to be 0.077−0.103 (average 0.1), 0.170−0.236 (average 0.2), and 0.237−0.288 (average 0.26) (Baud et al., 2017). Because porosity plays a first-order role in dictating physical properties such as sample strength and Young's modulus, the wide range of porosity found within a 10 mm-long sample questions the use of the average sample porosity when interpreting these data, and could help explain the large scatter in strength and Young's modulus when plotted as a function of sample porosity (Heap and Violay, 2021). In other words, samples with the same average sample porosity likely have different strengths simply due to whether the porosity is homogeneously or heterogeneously distributed throughout the sample. Finally, we note that the difference in porosity between that calculated from the stacked CT images and that measured in the laboratory (Fig. 7) implies that the dome samples studied herein contain significant microporosity (pores that are < 10 μm in diameter). This is particularly true for sample H4A (Fig. 7).

To conclude, and as discussed in Heap and Violay (2021), volcanic rocks are typically much more microstructurally heterogeneous than, for example, granites or sedimentary rocks. For example, the porosity of volcanic rocks can vary significantly (from almost 0 to almost 1), they can contain a wide distribution of pore sizes that can be characterised by different geometries (Shea et al., 2010; Zandomeneghi et al., 2010), they can contain both pores and microcracks (Kushnir et al., 2016), they can contain a variety of different types of crystals in different abundances that can be characterised by different crystal sizes, shapes, and size distributions (Cashman, 2020), their groundmass can be variably crystallised (Clarke et al., 2007; Zorn et al., 2018), and they can be variably influenced by hydrothermal alteration (Heap et al., 2021b).

4.2 Impact of heterogeneity on the strength of volcanic rocks and dome stability

Our calibrated 2D numerical experiments have shown that heterogeneity alone can reduce the uniaxial compressive strength of dome rock by more than a factor of two (Fig. 8). Previous modelling studies also found that microstructural heterogeneity leads to a reduction in rock strength (Tang et al., 2007, 2000; Zhu, 2008; Villeneuve et al., 2012; Ghazvinian et al., 2014; Peng et al., 2017; Liakas et al., 2017; Xu et al., 2020), and modelling designed to investigate the mechanical behaviour of volcanic rocks showed that pore size and shape (Heap et al., 2014b; Griffiths et al., 2017) and crystal content (Heap et al., 2016) can also influence rock strength. In the RFPA model, the numerical samples characterised by a high heterogeneity contain weaker elements (Fig. 3), which fail at lower stresses. The failure of a weak element results in a stress redistribution that can damage or fail neighbouring elements, even those with higher strengths. As a result, heterogeneity can provide weak elements, or weak zones, that can act as the locus for the formation of larger fractures that can result in macroscopic sample failure. In terms of a volcanic rock, microstructural heterogeneities such as pores and fractured crystals or, in the case of altered volcanic rocks, crystals that have suffered dissolution or partial or complete replacement with weak minerals such as clays, could act as the loci for damage that eventually results in macroscopic sample failure.

Our 2D dome simulations have shown that diffuse heterogeneity alone can promote lava dome instability (Fig. 10). Lava domes are structurally complex and comprise rocks with different strengths and, as such, are inherently heterogeneous. Our dome simulations (Fig. 10) highlight the need for not only assessing dome heterogeneity, but also monitoring processes that act to increase the heterogeneity of a dome, including processes that increase heterogeneity without changing the bulk strength of the dome. For example, the circulation of hydrothermal fluids may act to remove precipitates and/or sublimates within fractures in one part of the dome, resulting in weakening, which are then precipitated within fractures elsewhere in the dome, resulting in strengthening (although this will depend on the nature of the precipitated minerals). Although the bulk strength of the dome may not be greatly affected in this scenario, the increase in heterogeneity can weaken the entire structure, resulting in instability and potentially collapse.

Dome-scale displacement as a result of increased diffuse heterogeneity shows downward and outward movement of previously stable dome material (Fig. 10). This type of displacement was also found when modelling the stability of a dome containing a discrete zone characterised by a lower, but uniform, strength (Harnett et al., 2022), although displacement was focussed toward the flank of the dome where the weakened zone was located. We suggest, therefore, that small magnitude, but widespread, deformation of a lava dome may be the result of diffuse heterogeneity or may indicate a progressive increase in diffuse heterogeneity linked, perhaps, to a progressive increase in hydrothermal alteration.

Based on the results of our study, we suggest that existing numerical models that simulate discrete zones with different properties within a volcano need to also consider diffuse heterogeneity that might exist *within* these zones. Material heterogeneity in analogue experiments could also be considered by using, for example, sand-sized particles with different sizes and/or material properties. To demonstrate how discrete and diffuse heterogeneity could influence the results of numerical models of dome stability, we provide the dome-scale displacement and strain for (1) a homogenous dome with heterogeneous material properties ($m = 2$; Eq. 1) (Fig. 11a), (2) a dome with an internal, off-centre weak zone in which both discrete zones have uniform material properties (Fig. 11b; model results from Harnett et al., 2022), and (3) a dome with an internal, off-centre weak zone in which both discrete zones have heterogeneous material properties ($m = 2$; Eq. 1) (Fig. 11c).

For the homogeneous dome with heterogeneous material properties, deformation and fracturing can be observed on the flanks of the dome (Fig. 11a). Heterogeneous material properties induce an average displacement of 0.18 m, while the maximum displacement for any one particle is 0.87 m. As discussed in Harnett et al. (2022), a weak zone within the dome results in significant deformation and very large, dome-splitting fractures within and above the off-centre weakened zone when both discrete zones have uniform material properties (Fig. 11b). In this scenario, the introduction of a weakened discrete zone induces an average displacement of 0.29 m and a maximum displacement of 3.22 m. When uniform material properties are considered in the modelling, deformation is very much confined to the area adjacent to the weakened zone, and little to no deformation is observed on the opposite flank (Fig. 11b). When the model from Harnett et al. (2022) (Fig. 11b) is re-run but, this time, incorporating heterogeneous material properties in both zones ($m = 2$; Eq. 1), the deformation and fracturing within and above the off-centre weakened zone is reduced, but there is more deformation and fracturing on the opposite flank of the dome (Fig. 11c). The combined model showing both discrete and diffuse heterogeneity exhibits an average displacement of 0.36 m and a maximum displacement of 1.42 m. Interestingly, the strain resulting from the diffuse heterogeneity model (Fig. 11a) is not simply superimposed on the strain resulting from the discrete weakened zone (Fig. 11b): when diffuse heterogeneity is considered, a weakened zone on one side of the dome results in more fracturing on the opposite side of the dome (Fig. 11c). In other words, the introduction of diffuse heterogeneity in a dome that also contains a discrete weakened zone has resulted in damage that is more distributed throughout the dome, affecting a larger area, and less pronounced localisation in the form of dome-splitting fractures. This is because, when diffuse heterogeneity is considered, there are weak, failure-prone contacts throughout the dome that are not present when the material properties of the discrete zones are considered to be uniform. We speculate that, although a reduction in dome-splitting fractures may in the short-term reduce the probability of partial flank

collapses, distributed dome deformation may, in the long-term, mobilise larger volumes and promote larger-scale collapses.

These results highlight that deformation and fracturing within a dome may not necessarily indicate that there is a proximal weak zone, potentially complicating monitoring strategies at active lava domes. Further complications arise from the fact that this deformation pattern can be enhanced by the morpho-structural relationship between the dome and its surroundings (i.e. a buttressing effect provided by the paleo-collapse horseshoe-shape structure within which the dome was built or the inclination of the substratum of the dome; e.g., Heap and Harnett, 2021). Another important issue is the likely development of a collapse sequence with successive retrogressive slide blocks retreating into the dome. Our new modelling (Fig. 11) also suggests that future dome stability modelling should consider diffuse material property heterogeneity within discrete zones comprising the modelled dome. An estimation of the different rock masses potentially involved in different collapse scenarios (e.g., Peruzzetto et al., 2019) could also be refined to integrate the zonation of this dome heterogeneity. Ongoing research is now underway to develop strategies and methods to improve the capacity and resolution of static and functional imagery of volcanic domes (e.g., muon tomography and electrical conductivity), to find upscaling relations between numerical models and the geophysical characterisation scale, and to couple the results with thermo-hydro-mechanical simulations of fluid circulation within a lava dome.

Concluding remarks

The mechanisms considered responsible for dome instability and collapse are numerous and often operate in concert. Although the mechanisms may vary, understanding their impact on stability typically involves incorporating heterogeneity into the models, such as including material with a different rheology in analogue models (van Wyk de Vries et al., 2000; Cecchi et al., 2004) or by lowering the strength of material within a specific zone in numerical models (Harnett et al., 2022). The heterogeneities within these dome stability models are modelled as discrete zones with different, but uniform, material properties. These discrete zones could represent, for example, zones weakened by hydrothermal alteration, zones characterised by different rock types with disparate physical and mechanical properties, or zones characterised by a higher fracture density or pressurised fluids. Here, we consider the influence of diffuse heterogeneity on dome stability, motivated by the high heterogeneity of volcanic rock samples. In other words, although zones of discrete heterogeneities exist, there is also an underlying inherent heterogeneity in the material properties of a dome. Our numerical models show that this inherent diffuse heterogeneity can result in dome instability, highlighting that (1) domes are inherently

unstable, (2) dome instability can occur in the absence of obvious discrete weakened and/or fractured zones hence potentially producing volumes of unstable collapse-ready rock masses larger than otherwise expected, (3) when diffuse heterogeneity is considered, the impact of an off-centre weakened zone within the dome is more distributed throughout the dome (when compared to modelling that assumes uniform material properties for the discrete zones comprising the dome), and (4) future numerical modelling should consider heterogeneity within the discrete zones comprising the modelled dome. These results underscore the importance of understanding the range of volumes of material that can be involved in collapse scenarios. Furthermore, an increase in the heterogeneity in lava domes will likely reduce cohesion and, combined with other factors, may enhance the mobility of a collapse debris-avalanche, thereby increasing its runout and hazard potential. Understanding the mechanisms that can contribute to dome instability and collapse will help improve monitoring strategies and mitigate the hazards presented by lava domes worldwide.

Acknowledgements

This work was supported by ANR grant MYGALE ("Modelling the phYsical and chemical Gradients of hydrothermal ALteration for warning systems of flank collapse at Explosive volcanoes"; ANR-21-CE49-0010). M. Heap also acknowledges support from the Institut Universitaire de France (IUF). M. Heap and C. Harnett also acknowledge support from the Irish Research Council (IRC), the French ministries for Europe and foreign affairs (MEAE and higher education, research and innovation (MESRI), and Campus France via the Hubert Curien (PHC) Ulysses Ireland-France funding scheme. We thank The Fleet (Dublin, Ireland) for their hospitality. We thank IPGP for general funding to the Observatoires Volcanologiques et Sismologiques (OVS), the INSU-CNRS for funding provided by Service National d'Observation en Volcanologie (SNOV), and the French Ministère pour la Transition Ecologique et Solidaire (MTES) for financial support. The authors thank the OVSG-IPGP team for logistical support and help with data and material collection. This study contributes to the IdEx Université Paris Cité ANR-18-IDEX-0001. The comments of two reviewers, and the editor, helped improve this manuscript.

Statements and Declarations

The authors declare no financial or non-financial interests that are directly or indirectly related to this work.

Supplementary Information

Our manuscript is accompanied by two Supplementary Information files. Supplementary Information file 1 contains additional figures showing equivalent pore diameter, pore aspect ratio, and pore circularity as a function of sample length. Supplementary Information file 2 is an Excel spreadsheet containing the data for Figures 5, 6, 7, and 8.

Author contributions

M. Heap and C. Harnett conceived and developed the idea for this study. Numerical experiments using PFC were performed by C. Harnett. Numerical experiments using RFPA were performed by Z. Heng and T. Xu. Image analysis was performed by T. Nazarbayov. M. Heap and C. Harnett wrote the first draft of the manuscript, with contributions from all authors. All authors read and approved the final manuscript.

Figures

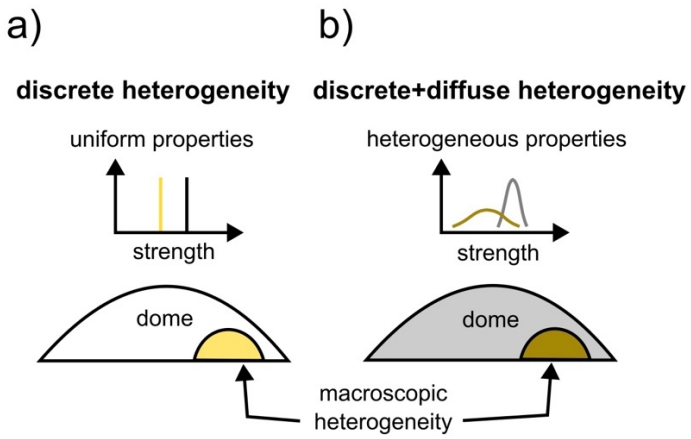

Fig 1. Schematic diagrams explaining the different types of lava dome heterogeneity discussed in this contribution. (a) Discrete heterogeneity: the lava dome is split into discrete zones (yellow and white) that are characterised by different, but uniform, physical and mechanical properties. (b) Discrete and diffuse heterogeneity: the lava dome is split into two discrete zones (dark yellow and grey) characterised by different physical and mechanical properties (discrete heterogeneity). In this case, the physical and mechanical properties within these zones are also heterogenous (diffuse heterogeneity).

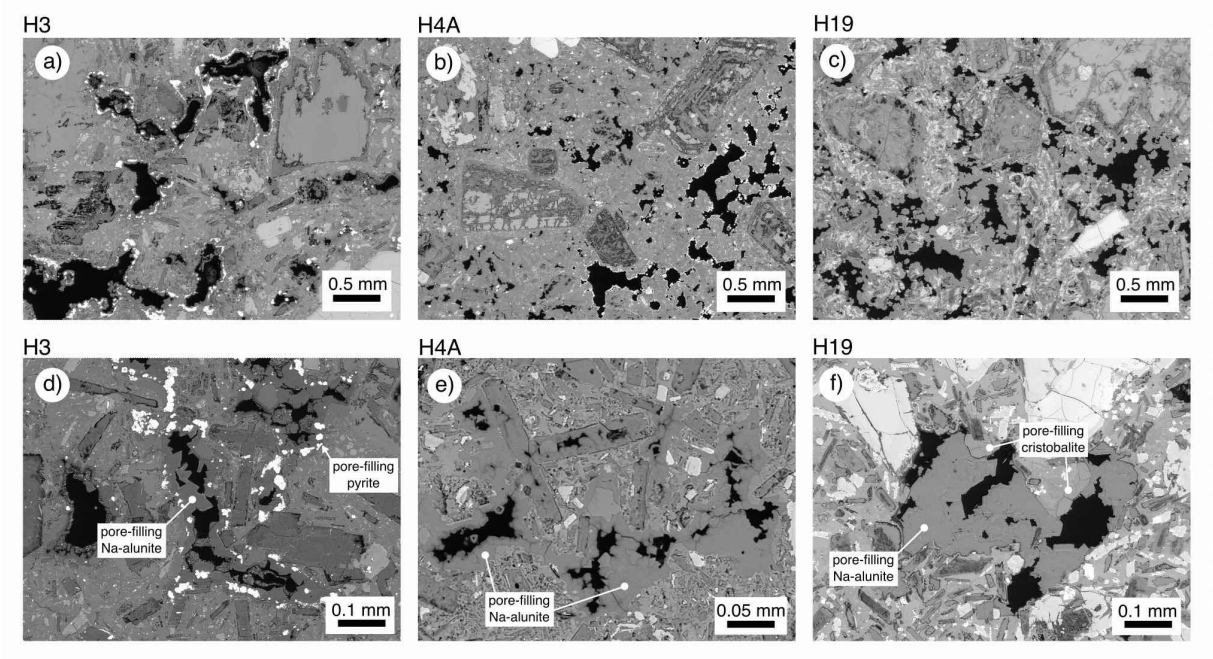

527

528 **Fig 2.** Backscattered scanning electron microscope images of the three dome rocks (H3, H4A, and H19) from La

529 Soufrière de Guadeloupe (Eastern Caribbean) analysed in this study. Black – void space; greyscale – groundmass

530 and crystals.

531

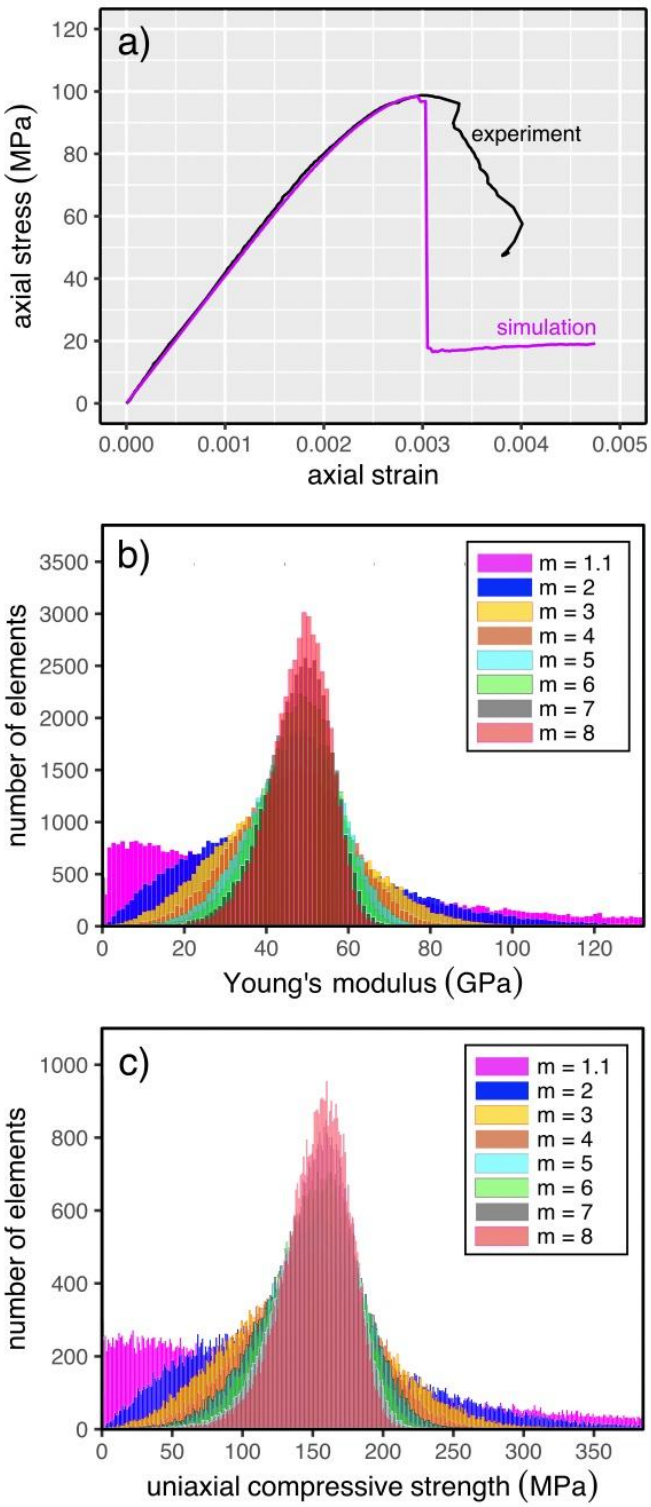

532

533 **Fig. 3.** (a) Uniaxial stress-strain curves from a laboratory experiment performed on an andesite sample (H18; data
534 from Heap et al., 2021b) (black curve) and from a numerical experiment using Rock Failure and Process Analysis
535 (RFPA). The parameters for the model (listed in Table 1) were modified until the modelled curve closely matched
536 the experimental data. Panels (b) and (c) show the distribution of Young's modulus and uniaxial compressive in a
537 numerical sample with a given homogeneity index, *m* (1.1, 2, 3, 4, 5, 6, 7, and 8).

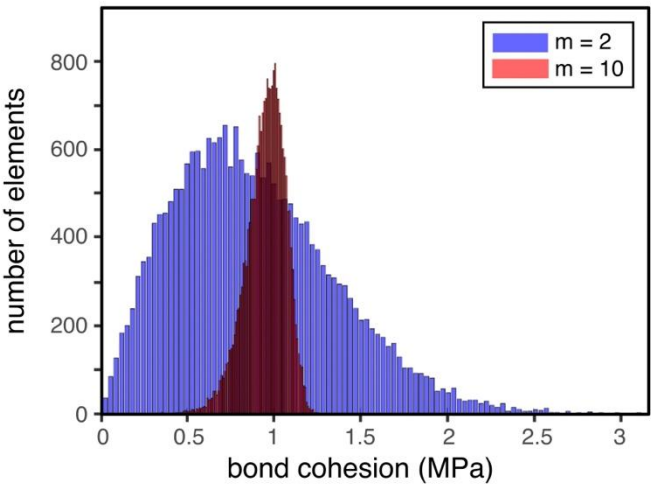

538

539 **Fig. 4.** The distribution of bond cohesion in the Particle Flow Code (PFC) domes characterised by different
540 homogeneity indices, m (the mean strength is 1 MPa in both cases). m = 2 (heterogeneous dome); m = 10
541 (homogeneous dome).

542

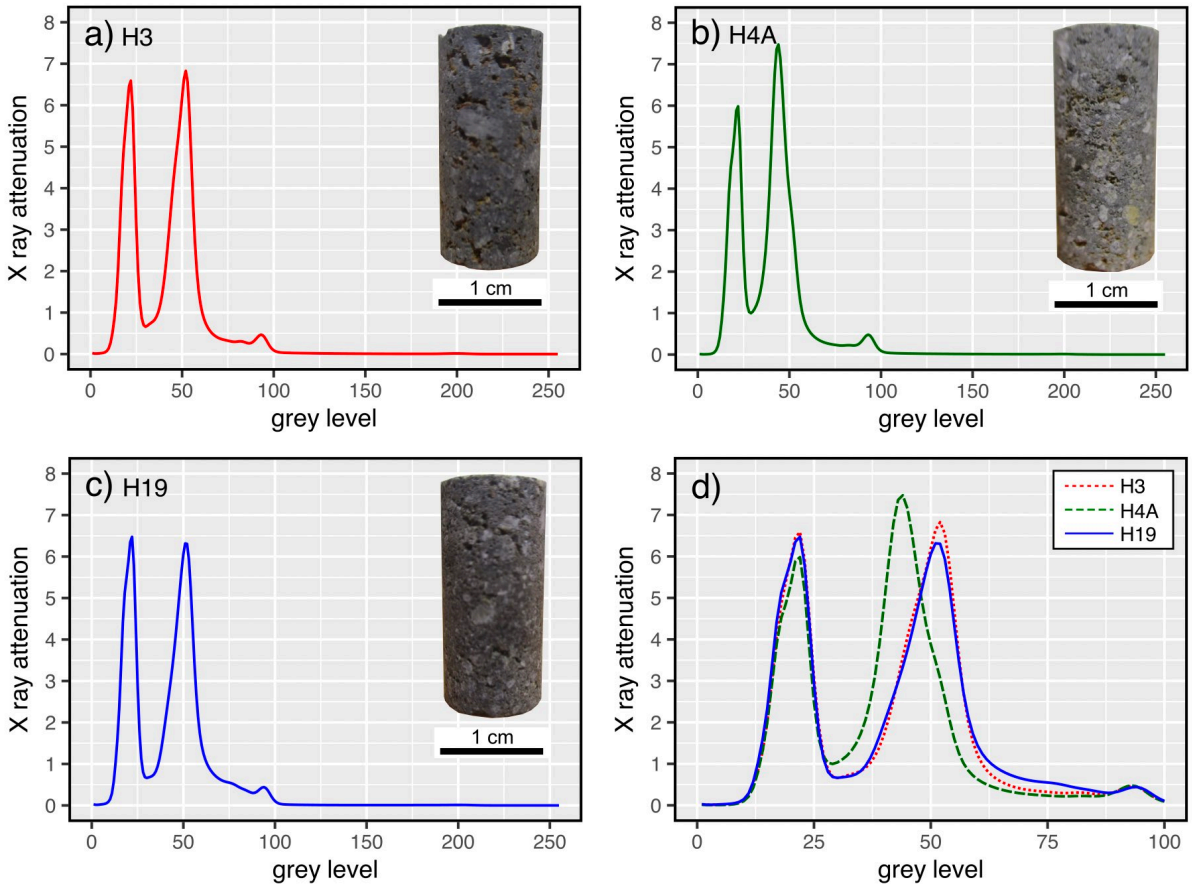

Fig. 5. Grey level histograms for three dome rocks from La Soufrière de Guadeloupe. Frequency is the relative frequency. (a) Sample H3. (b) Sample H4A. (c) Sample H19. (d) Synopsis plot containing all the data (note that the scale on x-axis is not the same as for the other panels). Insets show photographs of the 10 mm-diameter samples.

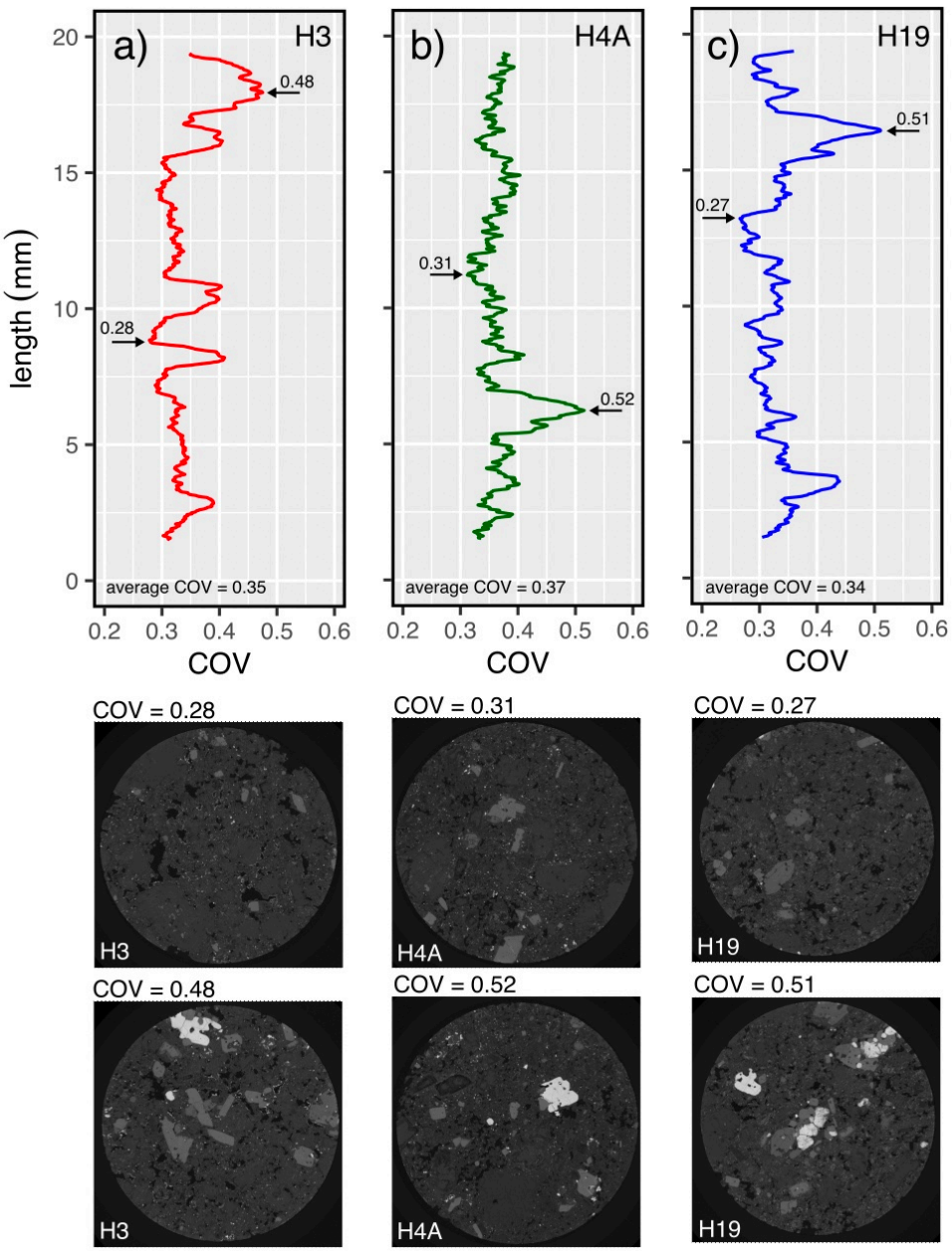

Fig. 6. The variation in coefficient of variation (COV) along the length of the 20 mm-long samples. (a) Sample H3. (b) Sample H4A. (c) Sample H19. The average COV and the location of the image slice with the highest and lowest COV are indicated on the plots. Below the plots are the image slices corresponding to the highest and lowest COV for each sample.

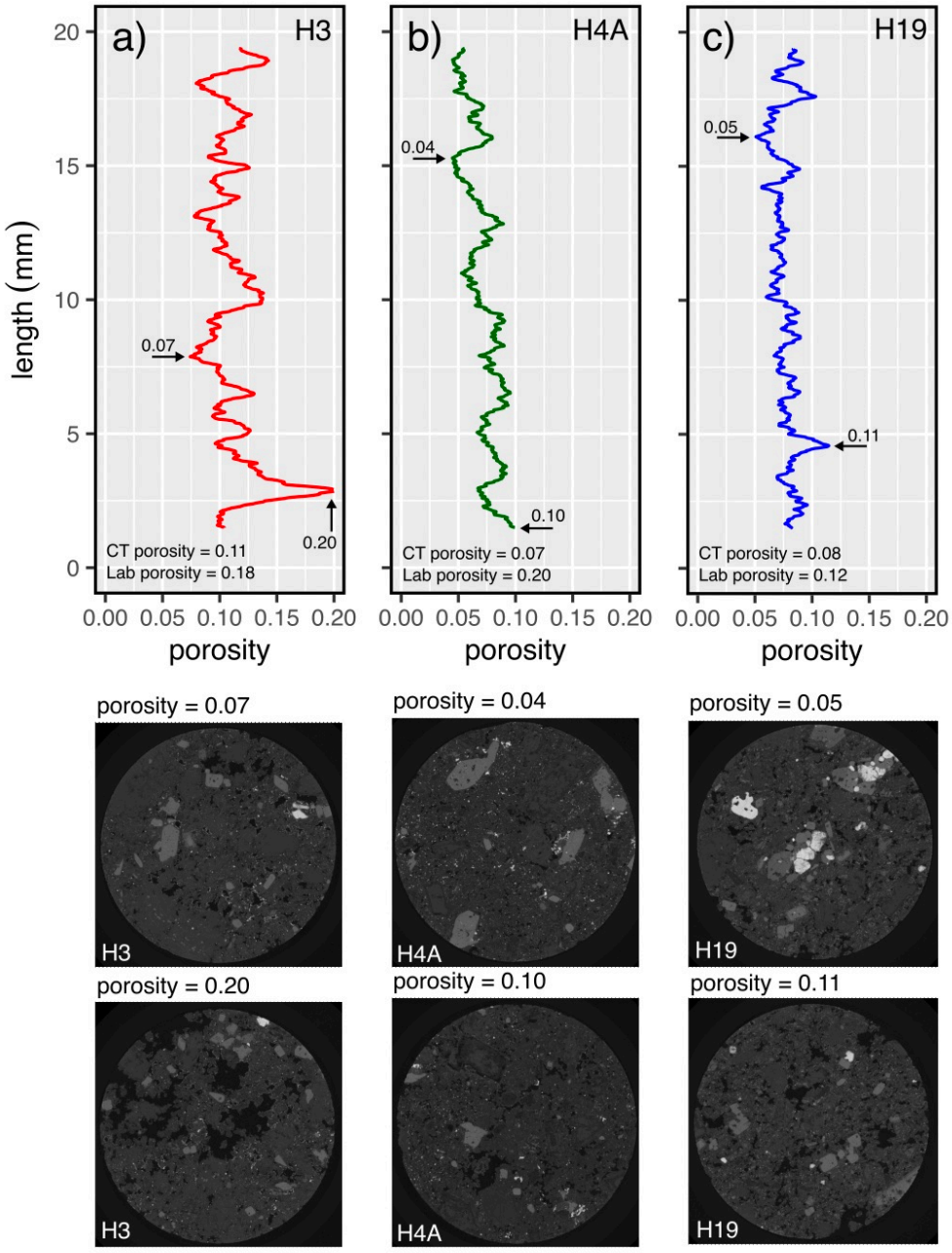

554

555 **Fig. 7.** The variation in porosity along the length of the 20 mm-long samples. (a) Sample H3. (b) Sample H4A. (c)
556 Sample H19. The average porosity (from the μCT volume and the laboratory) and the location of the image slice
557 with the highest and lowest porosity are indicated on the plots. Below the plots are the image slices corresponding
558 to the highest and lowest porosity for each sample.

559

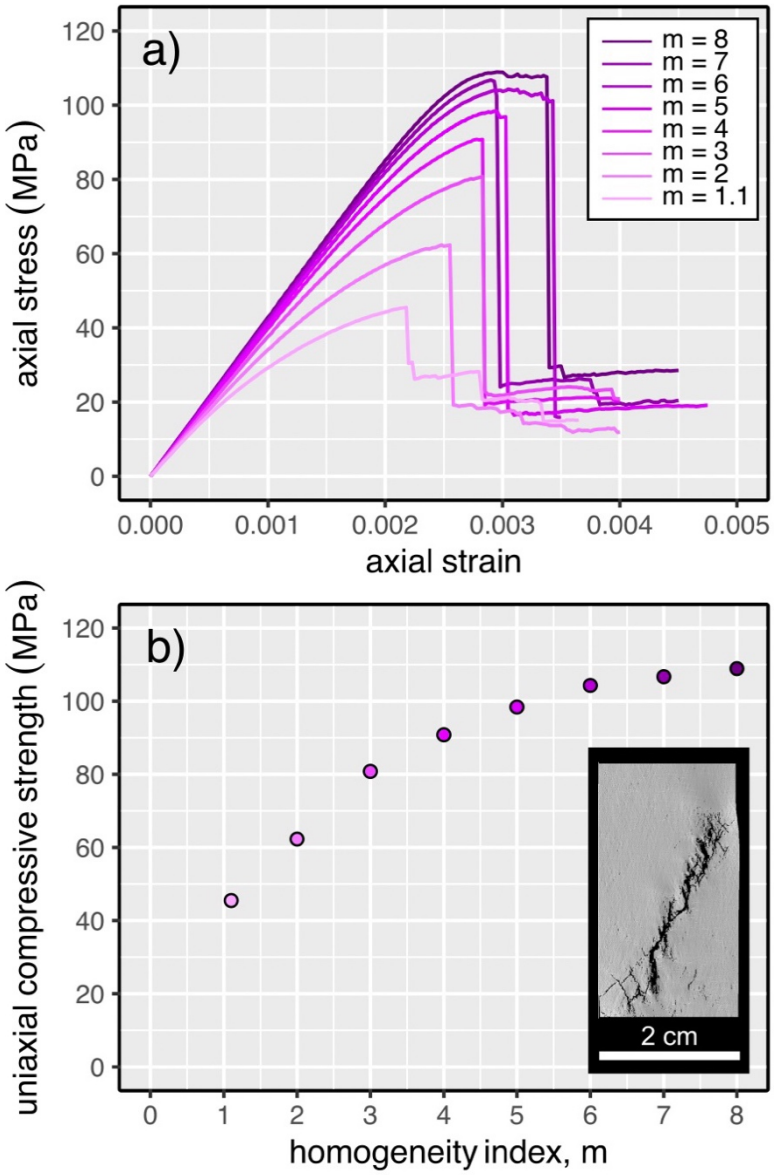

Fig. 8. Results of the 2D numerical experiments performed using Rock Failure and Process Analysis (RFPA). (a) Uniaxial stress-strain curves for numerical samples prepared with the same input parameters, but with different homogeneity indices (Table 1). The homogeneity index, m, varies from 8 (the most homogeneous sample) to 1.1 (the most heterogeneous sample). (b) Uniaxial compressive strength as a function of the homogeneity index (for the same numerical experiments shown in panel (a) (data available in Table 2). Inset shows an image of the post-failure numerical sample.

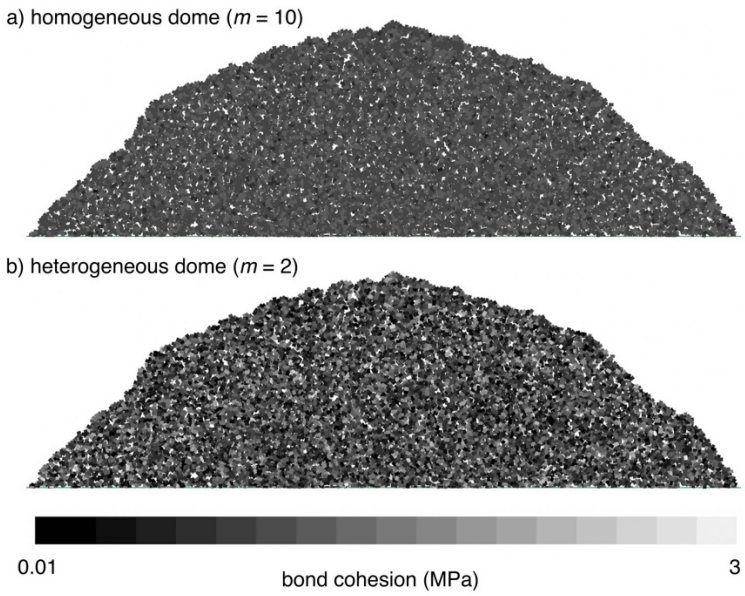

568

569 **Fig. 9.** Distribution of bond cohesion in (a) a homogeneous dome (m = 10) and (b) a heterogeneous dome (m = 2).

570 Dome width ~440 m.

571

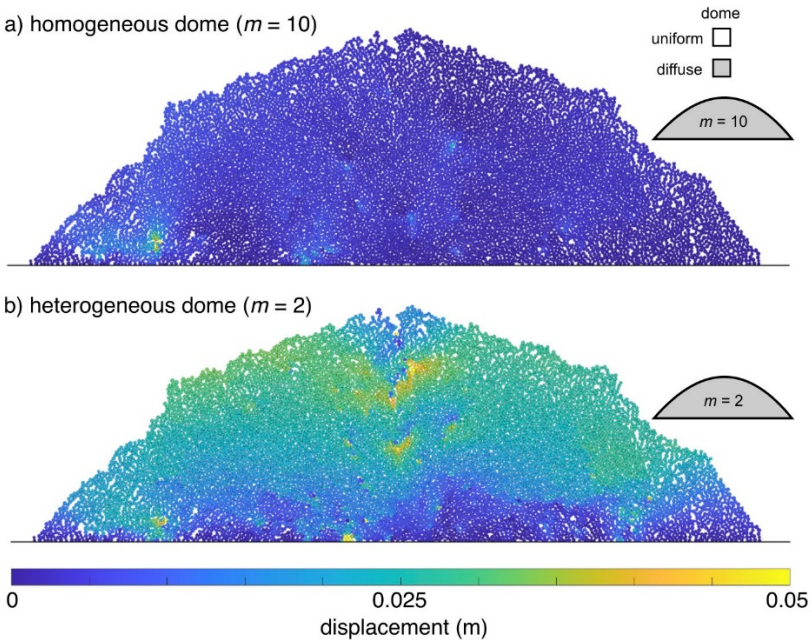

Fig. 10. Results of the 2D dome simulations (dome width ~440 m) performed using Particle Flow Code (PFC). (a) A homogeneous dome with a homogeneity index of 10. (b) A heterogeneous dome with a homogeneity index of 2. The colour indicates the displacement, where blue indicates low displacement and yellow indicates high displacement.

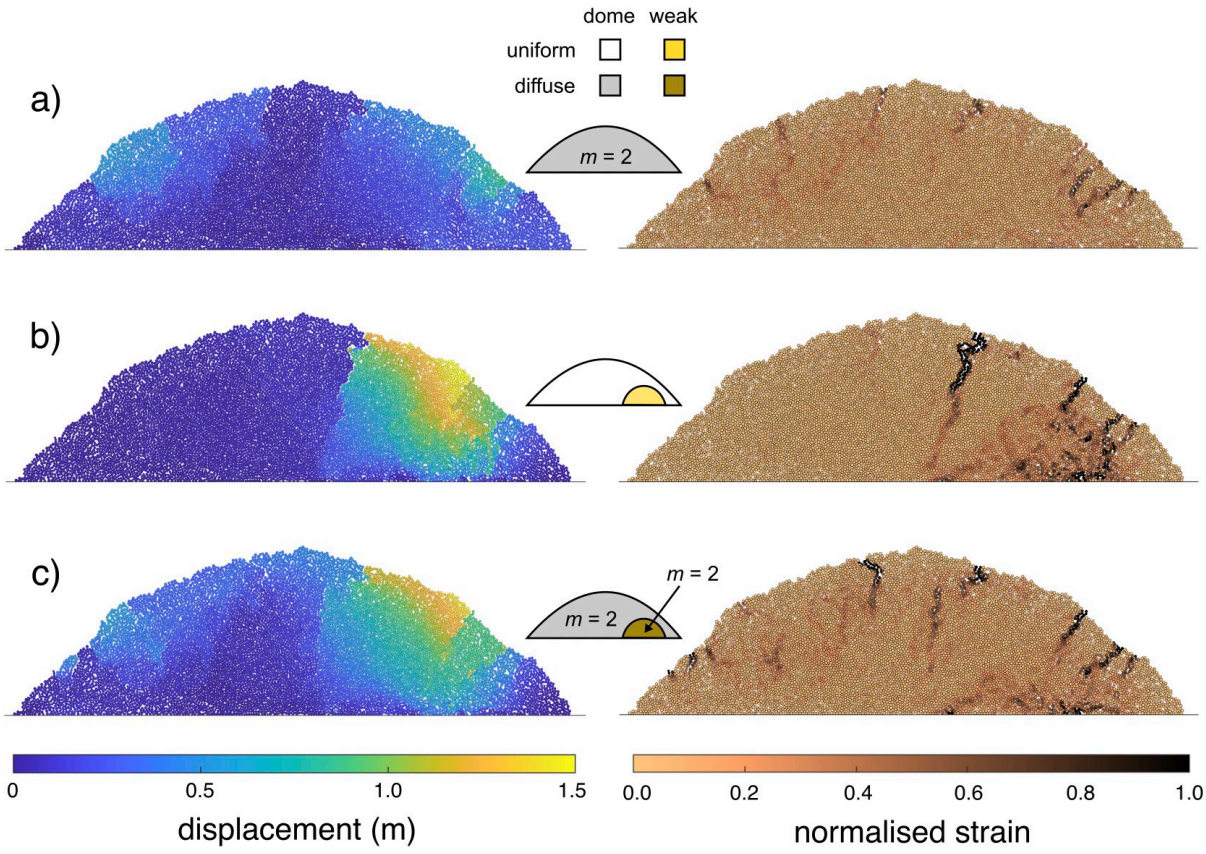

Fig. 11. Results of the 2D dome simulations (dome width ~440 m) performed using Particle Flow Code (PFC). Left plots show displacement from 0−1.5 m (yellow indicates higher displacement) and right plots show normalised strain, where darker areas indicate areas of high strain accumulation (dark brown indicates higher strain). (a) Dome with diffuse heterogeneity, as in Fig. 10. This dome is calibrated to unaltered rock as described by Harnett et al. (2022), with a heterogeneity index of $m = 2$, about a mean contact strength of 84.7 MPa. (b) Dome with a discrete zone of weaker material (both discrete zones have uniform material properties), identical to that presented by Harnett et al. (2022). (c) The combined effect of a discrete zone of weaker material *and* heterogeneous material properties in all zones. The dome rock is heterogeneous with $m = 2$ about a mean strength of 84.7 MPa and the weak rock is heterogeneous with $m = 2$ about a mean strength of 29 MPa. Thumbnail sketches of each scenario are provided in the middle of the modelled results.

591 **Tables**

592

Property	Value
Homogeneity index	1.1, 2, 3, 4, 5, 6, 7, 8
Mean uniaxial compressive strength (MPa)	147.3
Mean Young's modulus (GPa)	46.0
Poisson's ratio	0.25
Ratio of compressive to tensile strength	10
Friction angle (°)	30

593

594 **Table 1.** Model input parameters for the Rock Failure and Process Analysis (RFPA) modelling.

595

Homogeneity index, m	Uniaxial compressive strength (MPa)
8 (most homogeneous)	108.9
7	106.7
6	104.3
5	98.4
4	90.8
3	80.8
2	62.3
1.1 (most heterogeneous)	45.5

596

597 **Table 2.** Results of the 2D numerical experiments performed using Rock Failure and Process Analysis (RFPA).

598

References

Appoloni, C. R., Fernandes, C. P., & Rodrigues, C. R. O. (2007). X-ray microtomography study of a sandstone reservoir rock. Nuclear Instruments and Methods in Physics Research Section A: Accelerators, Spectrometers, Detectors and Associated Equipment, 580(1), 629-632.

Bain, A. A., Lamur, A., Kendrick, J. E., Lavallée, Y., Calder, E. S., Cortés, J. A., ... & Cortés, G. P. (2019). Constraints on the porosity, permeability and porous micro-structure of highly-crystalline andesitic magma during plug formation. Journal of Volcanology and Geothermal Research, 379, 72-89.

Ball, J. L., Calder, E. S., Hubbard, B. E., & Bernstein, M. L. (2013). An assessment of hydrothermal alteration in the Santiaguito lava dome complex, Guatemala: implications for dome collapse hazards. Bulletin of Volcanology, 75(1), 1-18.

Ball, J. L., Taron, J., Reid, M. E., Hurwitz, S., Finn, C., & Bedrosian, P. (2018). Combining multiphase groundwater flow and slope stability models to assess stratovolcano flank collapse in the Cascade Range. Journal of Geophysical Research: Solid Earth, 123(4), 2787-2805.

Baud, P., Exner, U., Lommatzsch, M., Reuschlé, T., & Wong, T.-f. (2017). Mechanical behavior, failure mode, and transport properties in a porous carbonate. Journal of Geophysical Research: Solid Earth, 122(9), 7363-7387.

Byrdina, S., Friedel, S., Vandemeulebrouck, J., Budi-Santoso, A., Suryanto, W., Rizal, M. H., & Winata, E. (2017). Geophysical image of the hydrothermal system of Merapi volcano. Journal of Volcanology and Geothermal Research, 329, 30-40.

Byrne, P. K., Holohan, E. P., Kervyn, M., van Wyk de Vries, B., Troll, V. R., & Murray, J. B. (2013). A sagging-spreading continuum of large volcano structure. Geology, 41(3), 339-342.

Calder, E. S., Luckett, R., Sparks, R. S. J., & Voight, B. (2002). Mechanisms of lava dome instability and generation of rockfalls and pyroclastic flows at Soufriere Hills Volcano, Montserrat. Geological Society, London, Memoirs, 21(1), 173-190.

Carr, B. B., Lev, E., Vanderkluysen, L., Moyer, D., Marliyani, G. I., & Clarke, A. B. (2022). The stability and collapse of lava domes: Insight from photogrammetry and slope stability models applied to Sinabung volcano (Indonesia). Frontiers in Earth Science, 10, 813813.

Cashman, K. V. (2020). Crystal size distribution (CSD) analysis of volcanic samples: advances and challenges. Frontiers in Earth Science, 8, 291.

Cecchi, E., van Wyk de Vries, B., & Lavest, J. M. (2004). Flank spreading and collapse of weak-cored volcanoes. Bulletin of Volcanology, 67(1), 72-91.

Clarke, A. B., Stephens, S., Teasdale, R., Sparks, R. S. J., & Diller, K. (2007). Petrologic constraints on the decompression history of magma prior to Vulcanian explosions at the Soufrière Hills volcano, Montserrat. Journal of Volcanology and Geothermal Research, 161(4), 261-274.

Darmawan, H., Walter, T. R., Brotopuspito, K. S., & Nandaka, I. G. M. A. (2018). Morphological and structural changes at the Merapi lava dome monitored in 2012–15 using unmanned aerial vehicles (UAVs). Journal of Volcanology and Geothermal Research, 349, 256-267.

Darmawan, H., Troll, V. R., Walter, T. R., Deegan, F. M., Geiger, H., Heap, M. J., ... & Müller, D. (2022). Hidden mechanical weaknesses within lava domes provided by buried high-porosity hydrothermal alteration zones. Scientific Reports, 12(1), 1-14.

Elsworth, D., Voight, B., Thompson, G., & Young, S. R. (2004). Thermal-hydrologic mechanism for rainfall-triggered collapse of lava domes. Geology, 32(11), 969-972.

Farquharson, J., Heap, M. J., Varley, N. R., Baud, P., & Reuschlé, T. (2015). Permeability and porosity relationships of edifice-forming andesites: a combined field and laboratory study. Journal of Volcanology and Geothermal Research, 297, 52-68.

Farquharson, J. I., Heap, M. J., Lavallée, Y., Varley, N. R., & Baud, P. (2016). Evidence for the development of permeability anisotropy in lava domes and volcanic conduits. Journal of Volcanology and Geothermal Research, 323, 163-185.

Fink, J. H., & Griffiths, R. W. (1998). Morphology, eruption rates, and rheology of lava domes: Insights from laboratory models. Journal of Geophysical Research: Solid Earth, 103(B1), 527-545.

Finn, C. A., Deszcz-Pan, M., Ball, J. L., Bloss, B. J., & Minsley, B. J. (2018). Three-dimensional geophysical mapping of shallow water saturated altered rocks at Mount Baker, Washington: Implications for slope stability. Journal of Volcanology and Geothermal Research, 357, 261-275.

Ghazvinian, E., Diederichs, M. S., & Quey, R. (2014). 3D random Voronoi grain-based models for simulation of brittle rock damage and fabric-guided micro-fracturing. Journal of Rock Mechanics and Geotechnical Engineering, 6(6), 506-521.

Gray, J. P., & Monaghan, J. J. (2004). Numerical modelling of stress fields and fracture around magma chambers. Journal of Volcanology and Geothermal Research, 135(3), 259-283.

Griffiths, L., Heap, M. J., Xu, T., Chen, C. F., & Baud, P. (2017). The influence of pore geometry and orientation on the strength and stiffness of porous rock. Journal of Structural Geology, 96, 149-160.
Harnett, C. E., Thomas, M. E., Purvance, M. D., & Neuberg, J. (2018). Using a discrete element approach to model lava dome emplacement and collapse. Journal of Volcanology and Geothermal Research, 359, 68-77.
Harnett, C. E., Thomas, M. E., Calder, E. S., Ebmeier, S. K., Telford, A., Murphy, W., & Neuberg, J. (2019a). Presentation and analysis of a worldwide database for lava dome collapse events: the Global Archive of Dome Instabilities (GLADIS). Bulletin of Volcanology, 81(3), 1-17.
Harnett, C. E., Kendrick, J. E., Lamur, A., Thomas, M. E., Stinton, A., Wallace, P. A., ... & Lavallée, Y. (2019b). Evolution of mechanical properties of lava dome rocks across the 1995–2010 eruption of soufrière hills volcano, Montserrat. Frontiers in Earth Science, 7, 7.
Harnett, C. E., & Heap, M. J. (2021). Mechanical and topographic factors influencing lava dome growth and collapse. Journal of Volcanology and Geothermal Research, 420, 107398.
Harnett, C. E., Heap, M. J., Troll, V. R., Deegan, F. M., & Walter, T. R. (2022). Large-scale lava dome fracturing as a result of concealed weakened zones. Geology, 50(12), 1346-1350.
Heap, M. J., Lavallée, Y., Petrakova, L., Baud, P., Reuschlé, T., Varley, N. R., & Dingwell, D. B. (2014a). Microstructural controls on the physical and mechanical properties of edifice-forming andesites at Volcán de Colima, Mexico. Journal of Geophysical Research: Solid Earth, 119(4), 2925-2963.
Heap, M. J., Xu, T., & Chen, C. F. (2014b). The influence of porosity and vesicle size on the brittle strength of volcanic rocks and magma. Bulletin of Volcanology, 76(9), 1-15.
Heap, M. J., Wadsworth, F. B., Xu, T., & Chen, C. F. (2016). The strength of heterogeneous volcanic rocks: a 2D approximation. Journal of Volcanology and Geothermal Research, 319, 1-11.
Heap, M. J., Villeneuve, M., Albino, F., Farquharson, J. I., Brothelande, E., Amelung, F., ... & Baud, P. (2020a). Towards more realistic values of elastic moduli for volcano modelling. Journal of volcanology and geothermal research, 390, 106684.
Heap, M. J., Baud, P., McBeck, J. A., Renard, F., Carbillet, L., & Hall, S. A. (2020b). Imaging strain localisation in porous andesite using digital volume correlation. Journal of Volcanology and Geothermal Research, 404, 107038.
Heap, M. J., Baumann, T., Gilg, H. A., Kolzenburg, S., Ryan, A. G., Villeneuve, M., ... & Clynne, M. A. (2021a). Hydrothermal alteration can result in pore pressurization and volcano instability. Geology, 49(11), 1348-1352.
Heap, M. J., Baumann, T. S., Rosas-Carbajal, M., Komorowski, J. C., Gilg, H. A., Villeneuve, M., ... & Reuschlé, T. (2021b). Alteration-Induced Volcano Instability at La Soufrière de Guadeloupe (Eastern Caribbean). Journal of Geophysical Research: Solid Earth, 126(8), e2021JB022514.
Heap, M. J., Wadsworth, F. B., Heng, Z., Xu, T., Griffiths, L., Velasco, A. A., ... & Deegan, F. M. (2021c). The tensile strength of volcanic rocks: Experiments and models. Journal of Volcanology and Geothermal Research, 418, 107348.
Heap, M. J., & Violay, M. E. (2021). The mechanical behaviour and failure modes of volcanic rocks: a review. Bulletin of Volcanology, 83(5), 1-47.
Heap, M. J., Harnett, C. E., Wadsworth, F. B., Gilg, H. A., Carbillet, L., Rosas-Carbajal, M., ... & Moretti, R. (2022a). The tensile strength of hydrothermally altered volcanic rocks. Journal of Volcanology and Geothermal Research, 107576.
Heap, M. J., Troll, V. R., Harris, C., Gilg, H. A., Moretti, R., Rosas-Carbajal, M., ... & Baud, P. (2022b). Whole-rock oxygen isotope ratios as a proxy for the strength and stiffness of hydrothermally altered volcanic rocks. Bulletin of Volcanology, 84(8), 1-14.
Heap, M. J., Jessop, D. E., Wadsworth, F. B., Rosas-Carbajal, M., Komorowski, J. C., Gilg, H. A., ... & Moretti, R. (2022c). The thermal properties of hydrothermally altered andesites from La Soufrière de Guadeloupe (Eastern Caribbean). Journal of Volcanology and Geothermal Research, 421, 107444.
Heiken, G., Wohletz, K., & Eichelberger, J. (1988). Fracture fillings and intrusive pyroclasts, Inyo Domes, California. Journal of Geophysical Research: Solid Earth, 93(B5), 4335-4350.
Husain, T., Elsworth, D., Voight, B., Mattioli, G., & Jansma, P. (2014). Influence of extrusion rate and magma rheology on the growth of lava domes: Insights from particle-dynamics modeling. Journal of volcanology and geothermal research, 285, 100-117.
Ji, Y., Hall, S. A., Baud, P., & Wong, T.-f. (2015). Characterization of pore structure and strain localization in Majella limestone by X-ray computed tomography and digital image correlation. Geophysical Journal International, 200(2), 701-719.
Kendrick, J. E., Schaefer, L. N., Schauroth, J., Bell, A. F., Lamb, O. D., Lamur, A., ... & Kennedy, B. M. (2021). Physical and mechanical rock properties of a heterogeneous volcano: the case of Mount Unzen, Japan. Solid Earth, 12(3), 633-664.
Komorowski, J-C., Hoblitt, R.P., Sheridan, M.F., 1997. Silicification and brecciation microtextures of the Mt. St. Helens 1980 cryptodome-country rock interface: implications for hydrothermal fluid processes, precursory

seismicity, and eruptive style. International Association of Volcanology and Chemistry of the Earth's Interior, General Assembly, Puerto Vallarta, Mexico, Jan. 19-25 1997, Abstract, p. 76

Komorowski, J. C., Jenkins, S., Baxter, P. J., Picquout, A., Lavigne, F., Charbonnier, S., ... & Budi-Santoso, A. (2013). Paroxysmal dome explosion during the Merapi 2010 eruption: Processes and facies relationships of associated high-energy pyroclastic density currents. Journal of Volcanology and Geothermal Research, 261, 260-294.

Krumbholz, M., Hieronymus, C. F., Burchardt, S., Troll, V. R., Tanner, D. C., & Friese, N. (2014). Weibull-distributed dyke thickness reflects probabilistic character of host-rock strength. Nature Communications, 5(1), 3272.

Kushnir, A. R., Martel, C., Bourdier, J. L., Heap, M. J., Reuschlé, T., Erdmann, S., ... & Cholik, N. (2016). Probing permeability and microstructure: unravelling the role of a low-permeability dome on the explosivity of Merapi (Indonesia). Journal of Volcanology and Geothermal Research, 316, 56-71.

Lagmay, A. M. F., Van Wyk de Vries, B., Kerle, N., & Pyle, D. M. (2000). Volcano instability induced by strike-slip faulting. Bulletin of Volcanology, 62(4), 331-346.Nakada, S., Shimizu, H., & Ohta, K. (1999). Overview of the 1990–1995 eruption at Unzen Volcano. Journal of Volcanology and Geothermal Research, 89(1-4), 1-22.

Lesparre, N., Gibert, D., Marteau, J., Komorowski, J. C., Nicollin, F., & Coutant, O. (2012). Density muon radiography of La Soufriere of Guadeloupe volcano: comparison with geological, electrical resistivity and gravity data. Geophysical Journal International, 190(2), 1008-1019.

Liakas, S., O'Sullivan, C., & Saroglou, C. (2017). Influence of heterogeneity on rock strength and stiffness using discrete element method and parallel bond model. Journal of Rock Mechanics and Geotechnical Engineering, 9(4), 575-584.

Liu, H. Y., Roquete, M., Kou, S. Q., & Lindqvist, P. A. (2004). Characterization of rock heterogeneity and numerical verification. Engineering Geology, 72(1-2), 89-119.

Long, H., Swennen, R., Foubert, A., Dierick, M., & Jacobs, P. (2009). 3D quantification of mineral components and porosity distribution in Westphalian C sandstone by microfocus X-ray computed tomography. Sedimentary Geology, 220(1-2), 116-125.

Louis, L., Baud, P., & Wong, T. F. (2007). Characterization of pore-space heterogeneity in sandstone by X-ray computed tomography. Geological Society, London, Special Publications, 284(1), 127-146.

Matthews, A. J., Barclay, J., Carn, S., Thompson, G., Alexander, J., Herd, R., & Williams, C. (2002). Rainfall-induced volcanic activity on Montserrat. Geophysical Research Letters, 29(13), 22-1.

Mériaux, C. A., May, D. A., & Jaupart, C. (2022). The impact of vent geometry on the growth of lava domes. *Geophysical Journal International*, *229*(3), 1680-1694.

Mordensky, S. P., Villeneuve, M. C., Kennedy, B. M., & Struthers, J. D. (2022). Hydrothermally induced edifice destabilisation: The mechanical behaviour of rock mass surrounding a shallow intrusion in andesitic lavas, Pinnacle Ridge, Ruapehu, New Zealand. Engineering Geology, 305, 106696.

Moretti, R., Komorowski, J. C., Ucciani, G., Moune, S., Jessop, D., de Chabalier, J. B., ... & Chaussidon, M. (2020). The 2018 unrest phase at La Soufrière of Guadeloupe (French West Indies) andesitic volcano: Scrutiny of a failed but prodromal phreatic eruption. Journal of Volcanology and Geothermal Research, 393, 106769.

Ogburn, S. E., Loughlin, S. C., & Calder, E. S. (2015). The association of lava dome growth with major explosive activity (VEI≥ 4): DomeHaz, a global dataset. Bulletin of Volcanology, 77(5), 1-17.

Peng, J., Wong, L. N. Y., & Teh, C. I. (2017). Influence of grain size heterogeneity on strength and microcracking behavior of crystalline rocks. Journal of Geophysical Research: Solid Earth, 122(2), 1054-1073.

Peruzzetto, M., Komorowski, J. C., Le Friant, A., Rosas-Carbajal, M., Mangeney, A., & Legendre, Y. (2019). Modeling of partial dome collapse of La Soufrière of Guadeloupe volcano: implications for hazard assessment and monitoring. Scientific Reports, 9(1), 13105.

Peterson, D. E., Finn, C. A., & Bedrosian, P. A. (2021). Airborne geophysical imaging of weak zones on Iliamna Volcano, Alaska: Implications for slope stability. Journal of Geophysical Research: Solid Earth, 126(3), e2020JB020807.

Reid, M. E., Sisson, T. W., & Brien, D. L. (2001). Volcano collapse promoted by hydrothermal alteration and edifice shape, Mount Rainier, Washington. Geology, 29(9), 779-782.

Reid, M. E. (2004). Massive collapse of volcano edifices triggered by hydrothermal pressurization. Geology, 32(5), 373-376.

Rhodes, E., Kennedy, B. M., Lavallée, Y., Hornby, A., Edwards, M., & Chigna, G. (2018). Textural insights into the evolving lava dome cycles at Santiaguito lava dome, Guatemala. Frontiers in Earth Science, 6, 30.

Rosas-Carbajal, M., Komorowski, J. C., Nicollin, F., & Gibert, D. (2016). Volcano electrical tomography unveils edifice collapse hazard linked to hydrothermal system structure and dynamics. Scientific reports, 6(1), 1-11.

776 Rosas-Carbajal, M., Jourde, K., Marteau, J., Deroussi, S., Komorowski, J. C., & Gibert, D. (2017). Three-
777 dimensional density structure of La Soufrière de Guadeloupe lava dome from simultaneous muon
778 radiographies and gravity data. Geophysical Research Letters, 44(13), 6743-6751.
779 Saucedo, R., Macías, J. L., Sheridan, M. F., Bursik, M. I., & Komorowski, J. C. (2005). Modeling of pyroclastic
780 flows of Colima Volcano, Mexico: implications for hazard assessment. Journal of volcanology and
781 geothermal research, 139(1-2), 103-115.
782 Shea, T., Houghton, B. F., Gurioli, L., Cashman, K. V., Hammer, J. E., & Hobden, B. J. (2010). Textural studies
783 of vesicles in volcanic rocks: an integrated methodology. Journal of Volcanology and Geothermal
784 Research, 190(3-4), 271-289.
785 Smith, R., Sammonds, P. R., Tuffen, H., & Meredith, P. G. (2011). Evolution of the mechanics of the 2004–2008
786 Mt. St. Helens lava dome with time and temperature. Earth and Planetary Science Letters, 307(1-2), 191-
787 200.
788 Sparks, R. S. J. (1997). Causes and consequences of pressurisation in lava dome eruptions. Earth and Planetary
789 Science Letters, 150(3-4), 177-189.
790 Sparks, R. S. J., & Young, S. R. (2002). The eruption of Soufrière Hills Volcano, Montserrat (1995-1999):
791 overview of scientific results. Geological Society, London, Memoirs, 21(1), 45-69.
792 Stavrou, A., Vazaios, I., Murphy, W., & Vlachopoulos, N. (2019). Refined approaches for estimating the strength
793 of rock blocks. Geotechnical and Geological Engineering, 37(6), 5409-5439.
794 Tanaka, H. K. M., Nakano, T., Takahashi, S., Yoshida, J., Ohshima, H., Maekawa, T., ... & Niwa, K. (2007).
795 Imaging the conduit size of the dome with cosmic-ray muons: The structure beneath Showa-Shinzan Lava
796 Dome, Japan. Geophysical Research Letters, 34(22).
797 Tang, C. (1997). Numerical simulation of progressive rock failure and associated seismicity. International Journal
798 of Rock Mechanics and Mining Sciences, 34(2), 249-261.
799 Tang, C. A., Liu, H., Lee, P. K. K., Tsui, Y., & Tham, L. (2000). Numerical studies of the influence of
800 microstructure on rock failure in uniaxial compression—part I: effect of heterogeneity. International
801 Journal of Rock Mechanics and Mining Sciences, 37(4), 555-569.
802 Tang, C. A., Tham, L. G., Wang, S. H., Liu, H., & Li, W. H. (2007). A numerical study of the influence of
803 heterogeneity on the strength characterization of rock under uniaxial tension. Mechanics of Materials,
804 39(4), 326-339.
805 Tang, S. (2011). Applications of rock failure process analysis (RFPA) method. Journal of rock mechanics and
806 geotechnical engineering, 3(4), 352-372.
807 Taron, J., Elsworth, D., Thompson, G., & Voight, B. (2007). Mechanisms for rainfall-concurrent lava dome
808 collapses at Soufrière Hills Volcano, 2000–2002. Journal of Volcanology and Geothermal Research, 160(1-
809 2), 195-209.
810 Tsepelev, I., Ismail-Zadeh, A., & Melnik, O. (2020). Lava dome morphology inferred from numerical modelling.
811 Geophysical Journal International, 223(3), 1597-1609.
812 Tuffen, H., Dingwell, D. B., & Pinkerton, H. (2003). Repeated fracture and healing of silicic magma generate flow
813 banding and earthquakes? Geology, 31(12), 1089-1092.
814 van Wyk de Vries, B., Kerle, N., & Petley, D. (2000). Sector collapse forming at Casita volcano, Nicaragua.
815 Geology, 28(2), 167-170.
816 Villeneuve, M. C., Diederichs, M. S., & Kaiser, P. K. (2012). Effects of grain scale heterogeneity on rock strength
817 and the chipping process. International Journal of Geomechanics, 12(6), 632-647.
818 Villeneuve, M. C., & Heap, M. J. (2021). Calculating the cohesion and internal friction angle of volcanic rocks
819 and rock masses. Volcanica, 4(2), 279-293.
820 Voight, B., Constantine, E. K., Siswowidjoyo, S., & Torley, R. (2000). Historical eruptions of Merapi volcano,
821 central Java, Indonesia, 1768–1998. Journal of Volcanology and Geothermal Research, 100(1-4), 69-138.
822 Voight, B. (2000). Structural stability of andesite volcanoes and lava domes. Philosophical Transactions of the
823 Royal Society of London. Series A: Mathematical, Physical and Engineering Sciences, 358(1770), 1663-
824 1703.
825 Voight, B., & Elsworth, D. (2000). Instability and collapse of hazardous gas-pressurized lava domes. Geophysical
826 Research Letters, 27(1), 1-4.
827 Wallace, C. S., Schaefer, L. N., & Villeneuve, M. C. (2022). Material properties and triggering mechanisms of an
828 andesitic lava dome collapse at Shiveluch Volcano, Kamchatka, Russia, revealed using the finite element
829 method. Rock Mechanics and Rock Engineering, 55(5), 2711-2728.
830 Walter, T. R., Subandriyo, J., Kirbani, S., Bathke, H., Suryanto, W., Aisyah, N., ... & Dahm, T. (2015). Volcano-
831 tectonic control of Merapi's lava dome splitting: The November 2013 fracture observed from high
832 resolution TerraSAR-X data. Tectonophysics, 639, 23-33.
833 Walter, T. R., Harnett, C. E., Varley, N., Bracamontes, D. V., Salzer, J., Zorn, E. U., ... & Thomas, M. E. (2019).
834 Imaging the 2013 explosive crater excavation and new dome formation at Volcán de Colima with

TerraSAR-X, time-lapse cameras and modelling. Journal of Volcanology and Geothermal Research, 369, 224-237.

Watts, R. B., Herd, R. A., Sparks, R. S. J., Young, S. R., & Druitt, T. H. (2002). Growth patterns and emplacement of the andesitic lava dome at Soufriere Hills Volcano, Montserrat. MEMOIRS-GEOLOGICAL SOCIETY OF LONDON, 21, 115-152.

Wong, T. F., Wong, R. H., Chau, K. T., & Tang, C. A. (2006). Microcrack statistics, Weibull distribution and micromechanical modeling of compressive failure in rock. Mechanics of Materials, 38(7), 664-681.

Xu, T., Zhou, G., Heap, M. J., Yang, S., Konietzky, H., & Baud, P. (2018). The modeling of time-dependent deformation and fracturing of brittle rocks under varying confining and pore pressures. Rock Mechanics and Rock Engineering, 51, 3241-3263.

Xu, T., Fu, T. F., Heap, M. J., Meredith, P. G., Mitchell, T. M., & Baud, P. (2020). Mesoscopic damage and fracturing of heterogeneous brittle rocks based on three-dimensional polycrystalline discrete element method. Rock Mechanics and Rock Engineering, 53(12), 5389-5409.

Zandomeneghi, D., Voltolini, M., Mancini, L., Brun, F., Dreossi, D., & Polacci, M. (2010). Quantitative analysis of X-ray microtomography images of geomaterials: Application to volcanic rocks. Geosphere, 6(6), 793-804.

Zhao, H., Zhao, T., Ning, Z., Zhang, R., Duan, T., Wang, Q., ... & Zhang, W. (2019). Petrophysical characterization of tight oil sandstones by microscale X-ray computed tomography. Marine and Petroleum Geology, 102, 604-614.

Zhu, W. C. (2008). Numerical modelling of the effect of rock heterogeneity on dynamic tensile strength. Rock mechanics and rock engineering, 41(5), 771.

Zhu, W. C., & Tang, C. A. (2004). Micromechanical model for simulating the fracture process of rock. Rock Mechanics and Rock Engineering, 37, 25-56.

Zorn, E. U., Rowe, M. C., Cronin, S. J., Ryan, A. G., Kennedy, L. A., & Russell, J. K. (2018). Influence of porosity and groundmass crystallinity on dome rock strength: a case study from Mt. Taranaki, New Zealand. Bulletin of Volcanology, 80(4), 1-17.

Zorn, E. U., Walter, T. R., Heap, M. J., & Kueppers, U. (2020). Insights into lava dome and spine extrusion using analogue sandbox experiments. Earth and Planetary Science Letters, 551, 116571.